Piezo-Phototronic In$_2$Se$_3$ Nanosheets as a Material Platform for Printable Electronics toward Multifunctional Sensing Applications

Christos Polyzoidis, Konstantinos Rogdakis,* George Veisakis, Dimitris Tsikritzis, Payam Hashemi, Hyejung Yang, Zdeněk Sofer, Ali Shaygan Nia, Xinliang Feng, and Emmanuel Kymakis*

A facile, ultralow-cost, and up-scalable printable manufacturing process of flexible, multifunctional sensors that respond to more than one external stimulus could have a pivotal role in low-cost wearables and portable systems for Industry 4.0. Herein, using a low capex, in-house spray coating system, the fabrication of a low-cost photodetector that is tuneable by mechanical strain exploiting the piezo-phototronic nature of defect-free 2D In$_2$Se$_3$ nanosheets is reported. Moreover, force sensors that respond to different levels of applied force are spray-coated by using In$_2$Se$_3$ nanosheets. Regarding the photodetector, a nonmonotonic and asymmetric effect of strain on photocurrent response is shown exhibiting a local maximum at the 23°–32° compressive angle range and a slight hysteresis. Forward compressive bending leads to a photocurrent enhancement by 27% at 32° and reverse by 31% at 23°, while tensile strain leads to a current suppression by 8–10% at 23°–32° angle. The resulting force sensor repeatably demonstrates discrete piezoelectric voltages in the millivolt scale upon different mass loads, opening the path for force and tactile sensing applications. Applying industrially compatible materials for the underlying flexible substrate and electrodes, combined with spray coating, removes manufacturing complexities that engage costly and energy intensive fabrication.

1. Introduction

The advent of the Internet of Things (IoT) implies the overwhelming flow of millions of data points from multiple sources and sensors[1,2] and builds upon a complex network connecting billions of devices and humans into a multiplatform infrastructure.[3,4] The ever-growing use of sensors in IoT networks renders the power consumption, processing speed, and system adaptation to be critical figures.[5] IoT system design may often include piezoelectric nanogenerators (PENGs) that have already been widely explored for several applications, including tactile sensing,[6–11] energy harvesting,[12–15] stress or strain sensing,[16–21] acoustic sensing,[22–26] as well as wearables.[27] Miniaturized integrated devices providing both mechanical strain and optical sensing in a single material stack could be thus a breakthrough technology by expanding the available sensing modalities.

2D materials (2DMs) are considered suitable candidates for miniaturized device concepts with high-performance optoelectronic functionalities due to their ultralow thickness reaching the atomic scale and the absence of dangling bonds.[28–32] One

C. Polyzoidis, K. Rogdakis, G. Veisakis, D. Tsikritzis, E. Kymakis
Department of Electrical & Computer Engineering
Hellenic Mediterranean University (HMU)
Heraklion 71410, Crete, Greece
E-mail: krogdakis@hmu.gr; kymakis@hmu.gr

K. Rogdakis, E. Kymakis
Institute of Emerging Technologies (i-EMERGE) of HMU Research Center
Heraklion 71410, Crete, Greece

P. Hashemi, H. Yang, A. Shaygan Nia, X. Feng
Faculty of Chemistry and Food Chemistry & Center for Advancing Electronics Dresden
Technische Universität Dresden
01062 Dresden, Sachsen, Germany

P. Hashemi, A. Shaygan Nia, X. Feng
Department of Synthetic Materials and Functional Devices
Max Planck Institute of Microstructure Physics
06120 Halle, Sachsen-Anhalt, Germany

Z. Sofer
Department of Inorganic Chemistry
University of Chemistry and Technology Prague
Technická 5, Prague 6 16628, Czech Republic

**ADVANCED
SCIENCE NEWS**

www.advancedsciencenews.com

**ADVANCED
MATERIALS
TECHNOLOGIES**

www.advmattechnol.de

of the most attractive attributes of 2D materials over their 3D counterparts is their mechanical stretchability, with a breaking strain typically above 10%.[33] Among them, 2DMs with formula A_2B_3 (where A stands for a group-III and B for a group-VI element, respectively) have been brought to researchers' attention due to their unique optoelectronic properties.[34–36] In_2Se_3 has a high absorption coefficient, broad range responsivity in the UV-NIR spectrum (e.g., 325–1800 nm), as well as high illumination sensitivity constituting an ideal material for optoelectronics applications.[37] Moreover, In_2Se_3 exhibits a thickness-dependent bandgap (from 1.3 eV in bulk crystal to 2.8 eV for a monolayer), and its electronic properties show significant advantages compared with gapless graphene and transition metal dichalcogenides (TMDs) that show relatively large bandgaps, E_g (1.5–2.5 eV) and only in the case of single layers.[38–42] As an additional comparative advantage over other air-sensitive direct-bandgap 2D materials (including black phosphorus[29]), intact In_2Se_3 flakes are highly stable in air.

Notably, Indium Selenides (such as a-In_2Se_3 and g-InSe) exhibit piezoelectric behavior while maintaining the same electrical polarization orientation between adjacent monolayers. This leads to increasing piezoelectric coefficients emergency as thickness increases.[43–45] It has been reported that the ferroelectric switching of a-In_2Se_3 can be controlled by electric fields (both drain and gate voltage biases in a transistor geometry), a process that is decoupled from photogenerated electron–hole pairs. Electrostatic gating was used to directly switch the in-plane polarization to out-of-plane.[46] The attractive coupled piezo-phototronic properties of In_2Se_3 outperform those of other 2D materials like graphene, black phosphorus, and MoS_2, and thus pave the way for research on the upscaled fabrication of high-quality photodetectors[47–50] and force sensors based on its unique piezo-phototronic properties.[51,52] Regarding flexible photodetectors, notable cases were reported in which In_2Se_3 was used in synergy with materials such as WSe_2,[53] rhombohedral (3R) MoS_2,[54] $CH_3NH_3PbI_3$ perovskite,[55] $SnSe_2$,[56] or used as the only active material.[57,58] Regarding In_2Se_3, available reports are based on techniques that are not cost effective and are labor intensive, such as transfer,[59,60] chemical vapor deposition (CVD),[51] or mechanical exfoliation on preconditioned substrate.[54] Photodetectors that are based in In_2Se_3 nanosheets yield a photosensitivity of up to 10^5 A W^{-1}. Their photoresponse is stable, fast, and reversible[37] and they promise to meet the demands of low-power detection of light such as in the example of underwater optical communications. Yet, top-performing devices mostly include CVD[61,62]-grown In_2Se_3 or employ small areas that contain a smaller amount of film defects thus the challenge of fabricating large volumes of defect-less In_2Se_3 flakes with large crystal domains hinders their practical applications.[51,57,59] On the other hand, force sensing based on 2D materials has been reported in literature.[63] Notable examples include devices based on MoS_2,[64,65] with reported gauge factors that exceed the respective ones of metal-based sensors (with values ranging between 1 and 5), graphene-based ($\approx$2),[66] doped-Si-based ($\approx$200),[67] or even exceeding the CNT-based sensors ($\approx$1000).[68] Regarding In_2Se_3-based force sensors, their applicability has been proven for healthcare and wearables,[43] or even as diaphragm material for FabryPerot fiber optic acoustic sensors.[69]

In_2Se_3 formulation is mostly achieved through micromechanical exfoliation, so that thin nanosheets with high quality are produced.[37,70] However, this technique has a low exfoliation yield, thus hindering its industrial upscaling.[71] Fabrication techniques to overcome this bottleneck include liquid phase exfoliation,[72] and wet-chemical synthesis[73,74] at the expense of the material's optoelectronic properties, such as lower photoresponsivity[71] and also resulting to increased defect density.[72,75] Promising upscaling techniques of In_2Se_3 ink fabrication attempt to alleviate this impediment[76] and can be applied to massively coat large areas and numbers of sensing elements without compromising material quality. Notably, a fast and scalable method bridging the gap between fundamental studies and industrial applications that decidedly reduces defects and yields solution-processable In_2Se_3 nanosheets, was recently developed by some of the authors that leverages cathodic intercalation in organic electrolytes.[76,77] An impressive exfoliation yield of 83% and In_2Se_3 sheets with lateral sizes up to 26 μm have been achieved within allegedly 30 min. It is notable that 68% of the exfoliated flakes comprised 3 layers and were 4 nm thin.[76]

The current work offers a facile, ultralow-cost and hence easily up-scalable way to fabricate In_2Se_3 flexible photodetectors tunable by mechanical stain as well as force sensors, both devices enabled by In_2Se_3 piezo-phototronic properties (**Figure 1**). The choice of industrially available materials for the underlying substrate and electrodes, as well as of the spray coating technique, removes manufacturing complexities that include active layer film transferring from one substrate to another, selecting and manipulating precursor materials, as well as engaging costly and energy intensive fabrication equipment. Finally, the In_2Se_3 ink has been selected for its stability and superiority concerning the absence of defects, large surface area and good optoelectronic properties. The present work's novelty is found on combining industrially upscalable fabrication techniques and a high quality 2DM ink of In_2Se_3 optimized for spray coating, while produced at large scales using industrially compatible methods.[76] The In_2Se_3 photodetector demonstrates onset (rise) and offset (decay) switching times in the range of ms (comparable to photodetectors developed on rigid substrates) and enhanced photoresponse for compressive mechanical strain at various bending angles. Mild compressive bending yields a higher photoresponse than the flat unbent state by up to 31% enhancement at 23° bending angle. Monotonic suppression of the photoresponse is reported by $\approx$10% compared to the unstrained case. On the other hand, the fabricated force sensor using a capacitor-like vertical structure of a In_2Se_3 film sandwiched between two electrodes, yields repeatable piezovoltage outputs that respond to different levels of applied force targeting diversified applications such as tough displays, tactile sensing, or force detection.

2. Results

2.1. Experimental Details

2.1.1. Electrochemical Exfoliation of In_2Se_3 and Ink Development

Cathodic electrochemical delamination of In_2Se_3 was performed using a 2-electrode system, as reported.[22] A crystal of α-In_2Se_3 (Ossila 99.999% purity) was chopped into $\approx$1 mm² pieces (nearly
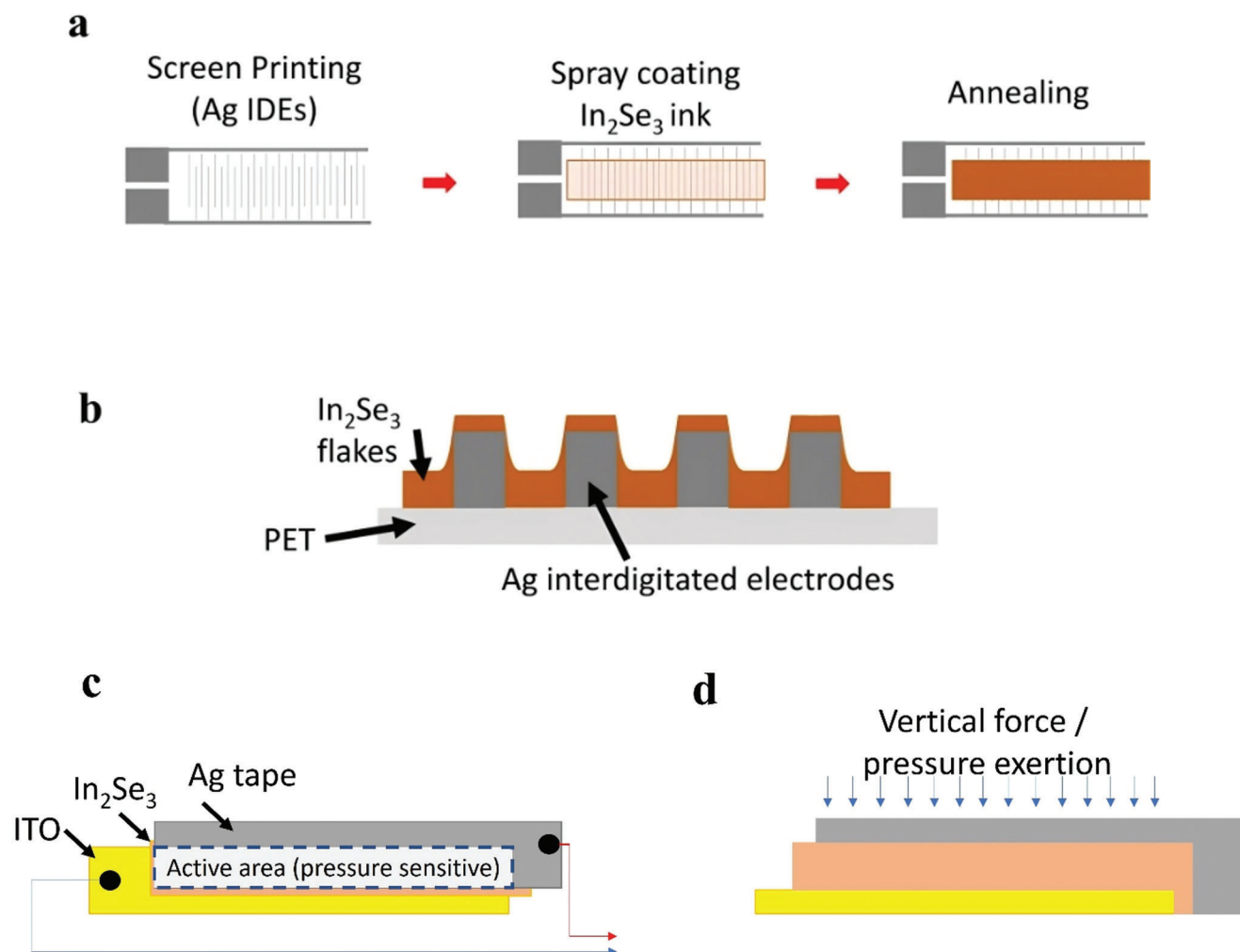
Figure 1. Overview of the manufacturing process of flexible photodetector and force sensing devices based on In_2Se_3 flakes. a) Top view of the fabrication process of the photodetectors including the IDEs fabrication, the spray coating of In_2Se_3 and the final annealing step. b) Side view of final material layer sequence of the photodetector (not-in-scale). This sketch is a part of the cross section alongside the long dimension of the sensor. c) Overview sketch of the In_2Se_3 based force sensor. This capacitor-like vertical structure functions as pressure sensor with the In_2Se_3 active layer sandwiched between two electrodes d) Lateral cross section view of the In_2Se_3 based force sensor.

50 mg) and placed in between a platinum gauze to serve as the cathode. A 1×3 cm^2 piece of Pt foil was used as the anode and placed 2 cm away from the cathode. The electrodes were submerged in a solution of 0.1 M tetrahexylammonium bromide (Sigma-Aldrich 99% purity) in N,N-dimethylformamide (DMF). A voltage of −5 V was applied to the crystals and the reaction was continued for nearly 30 min. The reaction workup was carried out by successive centrifugation at 5100 rpm for 5 min, discarding the supernatant, mixing the precipitate with 50 mL fresh DMF and centrifuging again (6 times). The final precipitate was centrifuged in 40 mL fresh DMF and centrifuged at 2000 rpm for 10 min to remove the unexfoliated particles and exfoliated thick layers. The supernatant, a stable dispersion of mono and few layer In_2Se_3 flakes in DMF (1 mg mL^{-1}), was collected. The dispersion was further diluted to 0.1 mg mL^{-1} for spray coating.

2.1.2. Device Fabrication

A heat-stabilized Polyethylene Terephthalate (PET) foil was chosen as the transparent substrate of the photodetectors and force sensing elements. For the photodetectors, interdigitated Electrodes (IDEs) were realized with screen-printing of Dupont PV410 silver (Ag) paste with a 120-sized polyester mesh and subsequent annealing at 140 °C for 30 min. A typical result of such IDEs is depicted on Figure S1a (Supporting Information). An ink of In_2Se_3 flakes dispersed in anhydrous DMF with a concentration of 0.1 mg mL^{-1} was spray coated on top of the IDEs for the formation of the active layer. The schematic in Figure 1(a) includes the top view of the sheet-to-sheet fabrication steps of the photodetectors while Figure 1(b) sketch demonstrates the layer sequence as it can be seen from a cross section alongside the long dimension of the device.

**ADVANCED
SCIENCE NEWS**

www.advancedsciencenews.com

**ADVANCED
MATERIALS
TECHNOLOGIES**

www.advmattechnol.de

Three different photodetectors were manufactured using either different total number of In_2Se_3 spray coating cycles (photodetectors I, II, and III) or different deposition technique (spray coating for photodetectors I, II, and III, while drop casting was used for photodetector IV). For the case of photodetector I, the total number of spraying cycles was set to 90 leading to a continuous In_2Se_3 layer with an approximate thickness of 140 nm. Finalized photodetector I is depicted in Figure S1b (Supporting Information). The total number of spraying cycles was set to 300 and 350 for the case of photodetector II and photodetector III, resulting to a thickness of 180 and 250 nm, respectively. During the spray coating process, the substrate was positioned on a hotplate inside a fume hood and constantly heated at 90 °C.

As a comparison, plain pipetting was used to fabricate another photodetector, no IV, with a layer thickness of about 1.9 μm. A picture of as-coated photodetector IV is depicted in Figure S1c (Supporting Information). Plain pipetting precisely positions ink and excludes probable ink wastage as in the case of a spray cone. However, drop-cast uneven dry films emerge due to uncontrolled solvent migration inside the wet film. This case is easier to be controlled with spray coating, even when an airbrush that yields inhomogeneous droplet sizes is used instead of more proper and expensive ultrasonic nozzles. Finally, upon annealing, wires were placed on the noncoated Ag electrode pads and fixed firmly with the aid of a silicone gun.

For the In_2Se_3 based force sensors, a commercially available PET/Indium–Tin Oxide (ITO) substrate was spray coated with a 50 nm thin In_2Se_3 film inside inert nitrogen atmosphere. Upon the ending of spraying procedure, the top electrode was placed by firmly and gently applying an Ag adhesive tape. Corresponding schematics of a top and side view of the force sensing elements manufacturing process are depicted in Figure 1(c,d), respectively, with a resulting total active area is 7.5 mm^2. Spray coating parameters were kept the same for photodetectors and force sensors. All images are not in scale. No encapsulation was applied in the present work confirming the high ambient stability of the reported devices.

2.1.3. Optoelectronic Characterization Setup and Procedure of Strain-Tunable Photodetector

Two 3D-printed sample holders that can host flexible samples were developed and used for the sake of testing. The one for larger bending angles can be seen in Figure S2b (Supporting Information) and the holder for lower angle measurements can be seen in Figure S2c (Supporting Information). Each sample is firmly fixed between two slots. The whole configuration can fit inside the lighting mini-chamber of Cicci research ARKEO measurement system and is depicted in Figure S2a (Supporting Information). All photodetectors are subjected to current-to-voltage ($I–V$) scanning under different bending and lighting conditions. Per each bending angle, $I–V$ scanning is followed by pulse testing under 3V bias voltage with a pulse duration of 3 s in order to check the temporal response of the photocurrent generation under periodic on/off light illumination. For the $I–V$ scanning case, photodetector's response is examined by linearly varying the bias voltage, while for the pulse mode, sensor's pulse response is examined under a constant 3 V bias. The choice of 3 V was arbitrary.

Moreover, absorbance measurements for the resulting In_2Se_3 thin film were performed with a ThetaMetrisis FRBasic system. Corresponding typical spectrograph can be seen in Figure S2d (Supporting Information) accompanied with an inset with the bandgap extraction plot.

2.1.4. Piezoelectric Voltage Response Characterization of Force Sensor

As far as the spray-coated In_2Se_3 functionality that is presented in Figure 1c,d is concerned, mechanical stress was initially applied perpendicularly to the surface. Three different forces were exerted by putting the respective loads of 50 g, 0.5 kg, and 1 kg on top of it. Then, a Keithley 2400 SMU was connected to the device electrodes and an inhouse datalogging software stored the output voltage values originating in the piezoelectricity of In_2Se_3. For each case, weights were manually loaded and unloaded in a very careful and delicate way so as not to create excessive sample stressing and unwanted piezovoltage surplus.

2.1.5. Thickness and Morphology Measurements

All thickness measurements were performed with a Veeco Dektak 150 profilometer and surface morphology was depicted with a ZEISS Gemini 500 Scanning Electron Microscope.

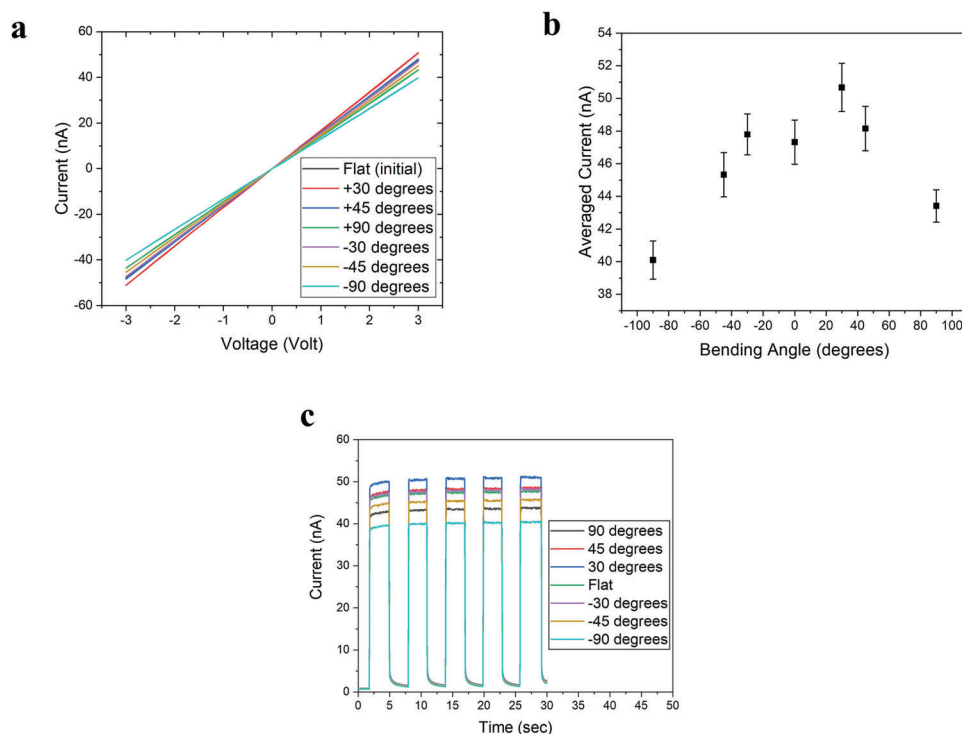### 2.1.6. Piezoelectric Force Microscopy (PFM) measurements

The PFM and topography images were acquired using the XE7 atomic force microscopy (AFM) from Park Systems and the SR830 lock-in amplifier from Stanford Research Systems. Electrically conductive Multi75E_G tips were employed for the measurements. The AC modulation voltage was set at 1 V. The scan rate was 0.2 Hz and the tip was in conduct mode. The In_2Se_3 flakes were deposited on ITO which was grounded during the PFM measurements.

2.2. Experimental Results

Regarding the In_2Se_3 nanosheet dispersion, relevant primary data on In_2Se_3 are included in the previous work of some of the authors.[76] Crystallographic data, Raman and X–ray photoelectron spectroscopy (XPS) spectra on In_2Se_3 nanosheet are presented in **Figure 2**b; and Figures S10 and S11 (Supporting Information) of the aforementioned work, respectively. UV–Vis spectroscopic data for the In_2Se_3 material are available in Figure S2d (Supporting Information) of the present work. Interested readers on further material properties should be redirected to the cited works by virtue of the different scope of the present study that focuses more on the device manufacturing and device novelty on the multifunctional sensing concept and less on the material's intrinsic properties.

2.2.1. Morphology of In_2Se_3 Flakes and Coated Films

We initially investigated the thickness and surface area distribution of the flakes as well as their typical surface roughness

**ADVANCED
SCIENCE NEWS**

www.advancedsciencenews.com

**ADVANCED
MATERIALS
TECHNOLOGIES**

www.advmattechnol.de

Figure 2. Mechanical strain effect on photodetector I output current at 1 Sun light illumination. a) Current-to-voltage curves under different bending angles. b) Photocurrent responses extracted from the I–V curves under different bending angles. c) Pulsed responses at 3 V bias and under different bending angles.

profiling. In Figure S3a (Supporting Information), a Scanning Electron Microscope (SEM) image of a coated In_2Se_3 film is depicted. In Figure S3b (Supporting Information) the statistical distribution of flakes lateral dimensions is extracted based on Figure S3a (Supporting Information). In Figure S3c (Supporting Information), an AFM topography is presented of a typical coated film indicating several flakes stacked one on top of another as well as a stepwise thickness change alongside the scanning direction across the film surface. The average surface area of the flakes is calculated to be around 8 μm. Although the root mean square (RMS) roughness of a single flake is sub-1 nm (inset of Figure S3c, Supporting Information), the effective film roughness ranges within few nanometers. Each step across the film corresponds to a different flake with a thickness of about 5 nm.
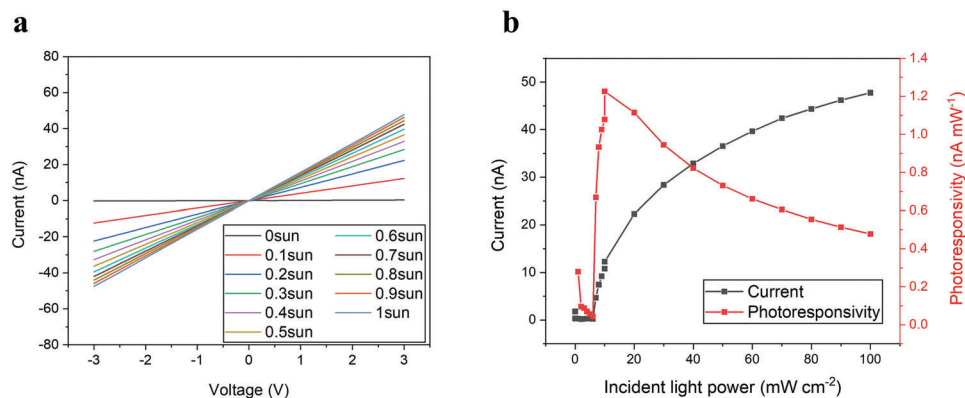
The morphology of the coated In_2Se_3 films of the various photodetectors was further investigated using SEM analysis. With regard to photodetector I, SEM characterization (Figure S4, Supporting Information) reveals overall a good coverage but at some points, especially on IDEs area where their surface roughness is very high, the In_2Se_3 film coverage is not adequate. Photodetector I is functional despite lacking in performance compared to its subsequent counterparts. It should be noted that SEM does not have the resolution to detect the ultrathin flakes of new nm in thickness. In contrast, a completely coated morphology is shown through SEM for the case of photodetector II (Figure S5, Supporting Information), III (Figure S6, Supporting Information), and photodetector IV (Figure S7, Supporting Information).

2.2.2. Piezoelectric Effect of the In_2Se_3 Films

The piezo/ferroelectric effect of the In_2Se_3 flakes was demonstrated by employing PFM. In specific, Figure S8b (Supporting Information) shows PFM image amplitude of In_2Se_3 film, while Figure S8c (Supporting Information) shows the corresponding PFM phase image. Different domains with different polarization vectors appear with different color intensity. Moreover, PFM tip poling experiments were also performed in order to study the piezo/ferroelectric hysteresis behavior of In_2Se_3 films. The amplitude response to the tip bias in Figure S9a (Supporting Information) shows a typical butterfly shape, whereas phase swift was also observed and hence depicted in Figure S9b (Supporting Information).[78] PFM amplitude and phase voltage hysteresis loops of In_2Se_3 flakes reveal a clear piezo/ferroelectric polarization behavior under an external electric field applied from the tip bias in agreement with literature reports. The presence of the unsaturated amplitude signal can be attributed to the substantial leakage, which results from a high concentration of free carriers in the samples. However, it cannot be ruled out that the surface charging effect might also be a contributing factor.[79]

2.2.3. Mechanical Strain Effect on Photodetector Output Current

The various photodetectors were initially tested under zero-angle, thus under flat, bending conditions. Subsequently compressive bending angles were tried with the following order: +30°, +45°, +90°. Finally, tensile bending angles were tried as follows: −30°,

2300203 (5 of 12)

**ADVANCED
SCIENCE NEWS**

www.advancedsciencenews.com

**ADVANCED
MATERIALS
TECHNOLOGIES**

www.advmattechnol.de

Figure 3. *I–V* characteristics of unbent photodetector I under different light intensities, a) from 0.01 to 1 Sun light intensities. b) Photoresponsivity (red colored) and photoresponse (black colored) values per different incident light power values for a given 3 V voltage bias under unbent conditions and using an nonmonochromatic warm white LED source.

−45°, −90°. The aim of this investigation was to identify the optimum combination of sensor's bending angle and irradiance value in order to maximize the sensor's response. The resulting Current-to-voltage (*I–V*) characteristics of photodetector I under 100 mW cm^{-2} irradiance is presented in Figure 2(a), while the electrical pulse averaged responses with error bars at different bending angles are shown in Figure 2(b) and the corresponding pulsed timeseries in Figure 2(c).

We investigated the effect of light illumination on the *I–V* characteristics of photodetector I initially at unbend conditions. Dimming the white Light Emitting Diodes (LEDs) of the measurement system (from dark to 1 Sun illumination conditions) helped to track the sensor's response per different light intensities (**Figure 3**a), while corresponding extracted photoresponsivity (red colored) and photoresponse (black colored) values per different incident light are depicted in Figure 3b. Although responsivity is usually considered a wavelength-dependent quantity, in the present case the effective responsivity for the nonmonochromatic light source of warm white LED illumination is calculated as the photocurrent per incident unit optical power.

A similar set of measurements were performed for photodetectors II-IV toward identifying the thickness dependence of the reported effects. The resulting *I–V* characteristics of the 180 nm thin photodetector II under light illumination of 100 mW cm^{-2} irradiance is presented in **Figure 4**.a, while the electrical pulse averaged responses with error bars at different bending angles are shown in Figure 4(b) and the corresponding pulsed timeseries in Figure 4(c).

The *I–V* measurements of the 250 nm thin photodetector III for different irradiances (ranging from 0 to 100 mW cm^{-2}) are depicted in **Figure 5**a and the corresponding calculated responsivities are depicted in Figure 5b. In order to test whether there is any hysteresis effect depending on the bending cycle procedure, bending tests and pulsed mode measurements were performed using two different protocols that both perform a fully closed bending cycle. Following the first protocol, samples were initially tested in flat state, namely under zero bending angle conditions. Subsequently, tensile bending was progressively applied from −12° to −45° that was followed by strain relax from −45° to −12° until zero bending angle. Thereafter, progressive compressive bending under different angles was applied from +12° until

45° and finally relaxation from +45° until again reaching the flat state. Figure 5c depicts the resulting hysteresis curve that consists of averaged responses under 3 V bias-pulses, as well as the corresponding statistical errors. Moving on to the second bending test protocol, we applied another bending cycle procedure, namely the initial unbent sample measurements were followed by progressive compressions from +12° to +45°, while being subsequently followed by gradual strain relax from +45° to the flat, zero-angle state. Then, progressive tensile bending from −12° to −45° was and a final relaxation from −45° until the flat state was performed. Figure 5d depicts the hysteresis curves that consist of averaged responses under 3 V bias-pulses for both respective bending cycles including the statistical errors.

Irrespective of whether bending test starts with compressive or tensile mode, a local maximum is evident in the small angle compression range. The bending angle for the maximized response differs, however, depending on the bending modes; When the process starts with tensile bending, then the sample exhibits a peak at 23° compressive bending angle (Figure 5c). On the other hand, when compressive strain is first applied the sample exhibits a peak response at 23°–32° angles (Figure 5d).

Figure S10 (Supporting Information) depicts pulsed timeseries for photodetector III during bending experiments with compression as first step of the first bending cycle. Figure S11 (Supporting Information) depicts subsequent tensile bending following the compressions. Figure S12 (Supporting Information) is the equivalent of Figure S8 (Supporting Information) for the second bending cycle. Figure S13 (Supporting Information) is the equivalent of Figure S11 (Supporting Information) for the second bending cycle and the final resting zero-angle state. In an attempt to develop a thick In$_2$Se$_3$ film, photodetector no. IV, was fabricated using a drop casting technique resulting in a layer with thickness of 1.9 µm. This device demonstrated a higher photoresponse under 100 mW cm^{-2} irradiance in the flat unbent state. Figure S14 (Supporting Information) depicts averaged pulse responses for the unbent Sensor IV at three distinct light intensities (1, 0.6, and 0.3-Sun). Overall, regarding the pulse height, most pulses were stable enough with a maximum error of −7 nA at 23° compressive state, 3 V pulses and ≈100 nA average pulse height in respect, as can be seen in the Supporting Information section. Average and error values in nA unit for both
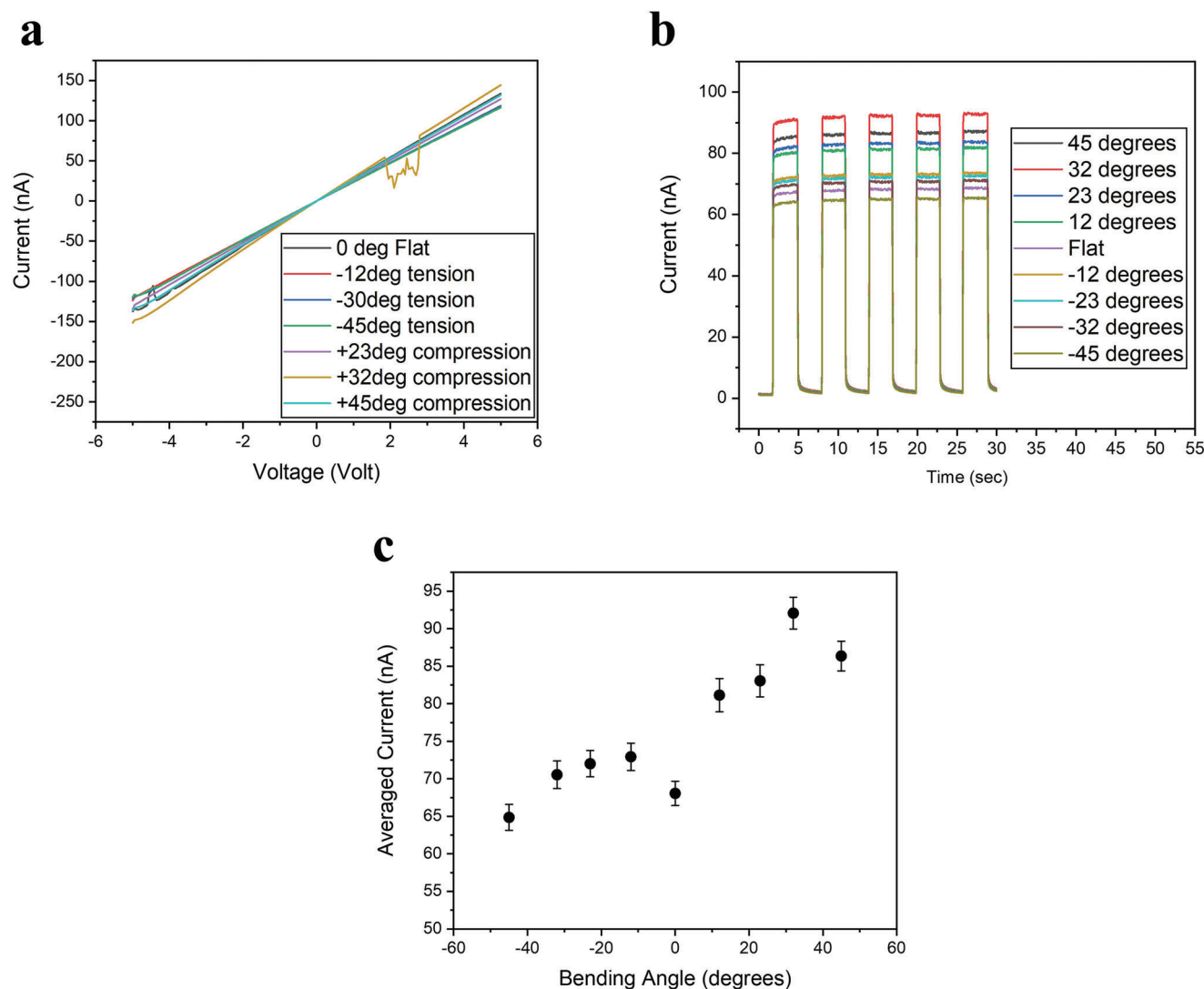
Figure 4. Mechanical strain effect on photodetector II output current at 1 Sun light illumination. a) Current-to-voltage curves under different bending angles. b) Pulsed responses at 3 V bias and under different bending angles. c) Photocurrent responses extracted from the *I–V* curves under different bending angles.
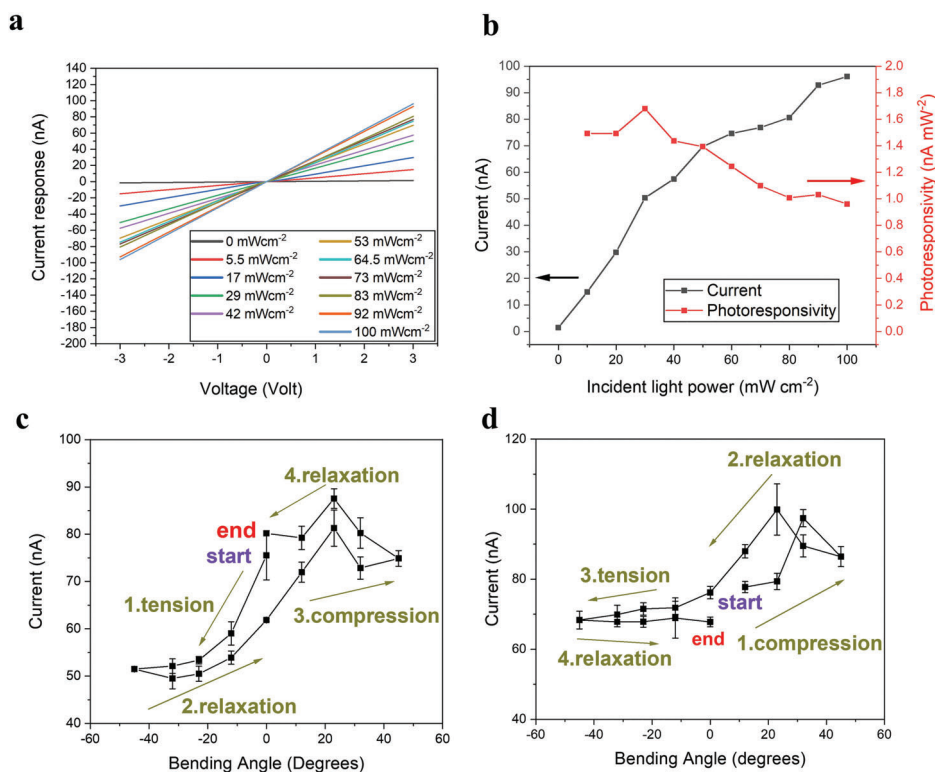
bending cycles are presented in Table S1 (Supporting Information). Figure S15a (Supporting Information) summarizes typical *I−V* response of all photodetectors in the unbent state under 100 mW cm^{-2} irradiance. Figure S15b (Supporting Information) includes the corresponding averaged pulsed responses for all four devices that are normalized according to their respective initial flat state responses. Figure S15c (Supporting Information) depicts the change in photoresponsivities per each photodetector for the unbent state under 100 mW cm^{-2} irradiance.

From what can be seen in the thickness dependencies in Figure S15b (Supporting Information), maximum normalized responses correspond to photodetectors II & III, namely samples with In$_2$Se$_3$ thicknesses 180 and 250 nm, respectively. As can be seen, tensile bending for all four photodetectors leads to a monotonic suppression of the photocurrent response, whereas applying mild compressive conditions all photodetectors exhibit an enhanced performance with a local maximum in the range of

≈20°. Finally, the 1.9 µm thick photodetector IV demonstrates the highest photoresponsivity of all four thickness cases because of the highest number of absorbed photons per light illumination.

2.3. The Potential Use of In$_2$Se$_3$ as Force Sensor

In order to further research the applicability of In$_2$Se$_3$ material as a multifunctional platform to other applications, we extend its use as a force sensing level. To this end, we have fabricated corresponding capacitor like structures as in Figure 1c,d. It is noted that all measurements correspond to indoor light conditions (warm white fluorescence lamps). **Figure 6**a presents the piezoelectric voltage response of the sensor when three different mass loads were periodically applied on its surface. Figure 6b depicts how average responses of multiple experiments change per different load applied to the force sensor. The statistics of relevant

**ADVANCED
SCIENCE NEWS**

www.advancedsciencenews.com

**ADVANCED
MATERIALS
TECHNOLOGIES**

www.advmattechnol.de

Figure 5. a) *I–V* measurements of photodetector III for different light intensities, b) measured current and calculated responsivities for the initially unbent photodetector versus light irradiances, c) the hysteresis curve including the statistical errors (in nA). Bending cycle starts with tension (negative angles). d) the hysteresis curve including the statistical errors (in nA). Bending test starts with compression (positive angles).

measurements and sensitivity calculations are presented in Table S2 (Supporting Information). Sensitivity is defined as the piezoelectric voltage per applied weight exerted (that can be converted to equivalent force) to the sensor's top surface.
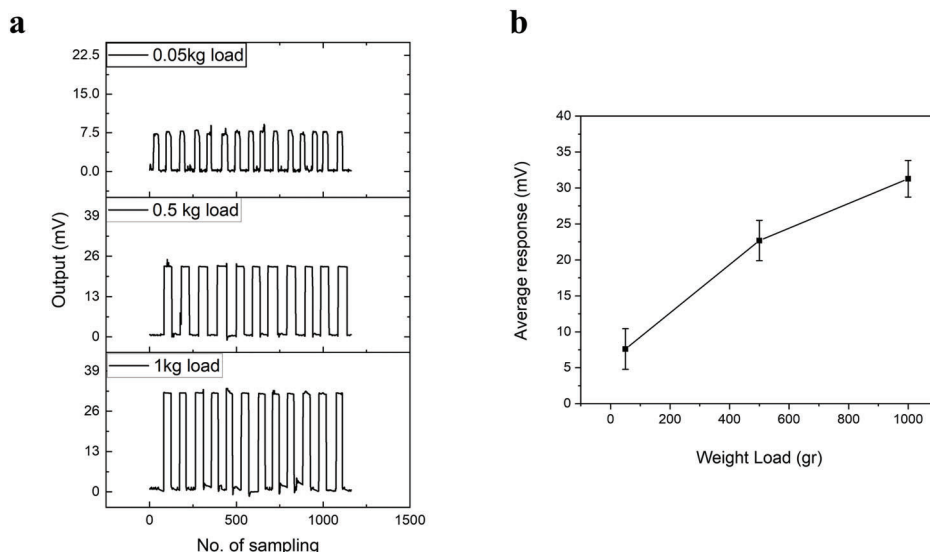
3. Discussion

This work demonstrates the good potential of In_2Se_3 flakes to be integrated as a multifunctional active material in various device concepts using low-cost, upscalable manufacturing techniques. To that end, two different device architectures were realized demonstrating a strain tunable photodetector and a force sensor using a thin layer of spray coated In_2Se_3 enabled by its unique piezo-phototronic properties.

For the strain tunable photodetectors, the substrate material was chosen to be the heat-stabilized and bendable PET that allows itself for processing temperatures up to 140 °C. The resulting film quality is satisfactory enough for yielding operational devices, but not the optimum one; spray (airbrush) coating on top of nonsmooth PET surfaces accounts for coarse In_2Se_3 films and definitely does not compete other deposition techniques in terms of film quality. This is a compromise that any upscaling engineer needs to meet unless the costly deposition equipment (such as industrial CVD) is available. On the other hand, in case an ultrasonic spray coater was used instead of an airbrush, droplet size would be more homogeneous, thus accounting for a smoother surface. However, equipment cost would be significantly higher

for mass production. Moreover, the screen-printed micrometer-thick Ag electrodes are easy to be upscaled by replacing flat-bed with rotary screen printing, but they still need to be further optimized in terms of geometry, namely interelectrode spacing, width, and number of the IDEs. Apart from these manufacturing points, we note that the higher the film thickness the stronger the measured photoresponse, however a tradeoff between material usage, scale down capability, and overall performance should be derived. No encapsulation was done on any of the sensors indicating the good lifetime stability of the active material. Upon upscaled production, an additional step for the sensors should include a barrier film roll that is unwind from an additional roll-to-roll unit, a laminator unit, and a final slicer.

On the other hand, the fabricated force sensors serve as an additional demonstrator for In_2Se_3 applicability potential. A thin active layer of ≈50 nm resulted to satisfactory and repeatable piezoelectric voltage signals upon excitation. Moreover, the top electrode tape application was done manually and was selected against the wet processing techniques in order to avoid damaging the thin In_2Se_3 layer, since coating the top electrode's material with any other wet technique led to In_2Se_3 film's perforation and ultimate device shunting. Besides, screen printing the top electrode with Ag paste would easily scratch the sample upon squeegee's pressure. A safer approach should include doctor blading of the conductive paste so as not to perforate the active layer but, again, such an upscaling step would require electrode patterning, usually via a laser scribing process that

ADVANCED
SCIENCE NEWS

www.advancedsciencenews.com

ADVANCED
MATERIALS
TECHNOLOGIES

www.advmattechnol.de

Figure 6. a) Generated piezovoltage upon application of perpendicular mechanical stress to In$_2$Se$_3$ surface. b) Scatter diagram including average responses and error bars per perpendicular load.

requires expensive equipment. Thus, resorting to applying a conductive tape means additional upscaling equipment, namely an unwinding unit for the conductive tape, a lamination unit that exerts optimized pressure to the tape in order to firmly attach to In$_2$Se$_3$ surface without damaging the film or encapsulating any trapped air, as well as a cutting unit that mechanically scribes the samples. Elsewise, higher In$_2$Se$_3$ thicknesses might allow for top electrode coating instead of tape application.

As a final upscaling concern, In$_2$Se$_3$ dispersion must be coated and annealed inside an inert atmosphere, while the rest steps can be performed at ambient conditions. This necessity is translated into industrial practice by employing a dedicated chamber that is filled with inert gas (pure N$_2$ or Argon) and hosts the spraying system as well as an additional section that hosts drying units, most notably by applying hot dry air,[80] or UV treatment. Contrary to this, in the present work a hot plate was used that does not comply with the need for upscalability.

Moreover, the unencapsulated photodetectors proved to be modestly stable under ambient conditions (40–60% RH). Consecutive measurements that are distanced by tens of hours exposure show ambient stability of the sensor that needs to be further protected, although performing systematic bending and stability measurements, as well as exposing and controlling the sensor's stability mechanisms was not the essence of this work. On the other hand, the capacitor-like force sensors do not demonstrate any significant degradation concerns upon ambient exposure since the top electrode tape covers the underneath In$_2$Se$_3$ layer. Moreover, ambient exposure may take its toll on overall performance, since water decomposition at Se vacancies has been reported that occurs at room temperature at a high rate.[81] On top of that, Se vacancies on an exposed film's surface may react with moisture and oxygen and consequently result to further oxidation of neighboring In–Se bonds on the basal plane, thus leading to a more grave degradation, as it has been reported for the case of InSe.[82] Oxygen may lead also to formation of In$_2$O$_3$ at In$_2$Se$_3$ monolayer surface, although in the case of In$_2$Se$_3$ no

alterations on band structure had been observable. As future directions, in order to cancel ambient adverse effects, the canceling of the presence of Se vacancies by filling them with S atoms through a further CH$_3$SH treatment of InSe surface, as already suggested[83] may complement the much needed encapsulation step.

The focus of our study was to investigate how the optoelectronic properties of In$_2$Se$_3$ films are affected by static strain conditions (we applied constant bending angles on the films, but not dynamic bending cycles). Nonetheless we tested the unencapsulated device stability after 100 bending cycles and noticed a slight change in the current, as evidenced in Figure S16 (Supporting Information). It has also been found that subsequent strong bending cycles impose a degradation of the device performance. Extreme bending states that exceed the (−90°, +90°) range easily degrade the sensor, most probably due to delamination among materials at the In$_2$Se$_3$/PET interface and other inflicted material discontinuities, such as the cracks on the In$_2$Se$_3$ morphology. Under mild bending conditions within the lower angle range, the In$_2$Se$_3$ photodetector may yield repeatable results and be customized for specific applications that combine optoelectronic and mechanical constraints (see additional characterization methods in the Supporting Information including visual inspection and adhesion testing of In$_2$Se$_3$ films). With regard to the force sensor case, however, any bending radius beyond ITO manufacturer's specifications is expected to irreversibly damage the ITO electrode and account for cracks on its surface that will deteriorate its electrical properties. Making a final remark on the force sensor, sensitivity values are not in accordance with force sensing state-of-the-art performance and still a device optimization is required. For instance, the demonstrator force sensor yields sensitivities comparable to flexible piezoelectric force sensors based on Polyvinylidene Fluoride (PVDF) fabric of older research[46] but still lacks against more recent comparable works.[84] Besides, it has not been tested against a sufficiently high number of stress repetitions.[85]

**ADVANCED
SCIENCE NEWS**

www.advancedsciencenews.com

**ADVANCED
MATERIALS
TECHNOLOGIES**

www.advmattechnol.de

Last but not least, the very issue of adopting a standardized characterization procedure in relevant future research works is vital toward securing the market uptake of upscaled In_2Se_3 sensing functionalities. Abiding by a proper measurement and data reporting protocol for standardizing data collection and analysis for piezoelectric energy harvesting devices, such as the one that was recently suggested by Amiri, Morteza Hassanpour et al.,[86] is expected to enhance reproducibility in this research field, hence further paving the way for the mass production of robust and reliable In_2Se_3-based sensing and harvesting functionalities.

4. Conclusion

This work has first resulted to strain tunable photodetectors that yield reproducible and thus predictable behavior, under mild compressive conditions within the lower angle range, thus rendering the In_2Se_3 sensor suitable to be customized for specific applications that combine optoelectronic and mechanical stimuli. Therefore, the effect of repeating hundreds of bending cycles, the emergence of bending angle shifts, the effect of proper encapsulation on finalized sensor's performance, as well as the better understanding of In_2Se_3 sensor hysteresis and asymmetries are issues that remain to be explored. Moreover, this work demonstrated that a In_2Se_3-based force sensor has repeatable piezoelectric voltage responses upon several loads that indicate a promising future for the material's uses in force and tactile sensing applications. In addition, upon integrating this device in appropriate circuits, piezoelectric energy harvesters can be developed.[44]

The fabricated photodetectors and force sensors do not still compete in terms of performance other state-of-the-art devices that operate distinctly either as photodetectors or force sensors. On the contrary, the current study stress on the multifunctional role of In_2Se_3 flakes that is a clear advantage compared to other systems. This material platform can be used as a multifunctional sensing element that in principle can be used to detect various stimuli at the same time. Moreover, our approach constitutes a cost effective approach in terms of profitability for the end user by virtue of the low cost materials (commercially available PET foil, low cost In_2Se_3 flake dispersion), low material consumption (screen printing prevents silver paste material's wastage and multiplies the number of batches fabricated with the same, recycled paste quantity), ultralow energy consumption (no vacuum or high temperature fabrication steps are required), as well as its fabrication simplicity and repeatability (since no film transfer or other manually performed task that necessitates delicate or sophisticated handling is necessary). Thus, the competitive edge of this work lies within its cost effectiveness and low capex for establishing an according mass-production line, an oversimplified example of which is depicted in Figure S17 (Supporting Information) that includes a roll-to-roll line for the sensor's necessary materials deposition.

Last but not least, the physics detailed investigation of the developed sensors (see a preliminary discussion in the Supporting Information note) will follow up in a future work and will constitute a crucial step toward in-depth understanding of their underlying mechanisms, their response optimization, as well as their final competitive edge over similar functionalities that are commercially available in present time.

Supporting Information

Supporting Information is available from the Wiley Online Library or from the author.

Conflict of Interest

The authors declare no conflict of interest.

Data Availability Statement

The data that support the findings of this study are available from the corresponding author upon reasonable request.

[1] R. Haight, W. Haensch, D. Friedman, *Science.* **2016**, *353*, 124.
[2] H. Yasuura, C. M. Kyung, Y. Liu, Y. L. Lin, *Smart Sensors at the IoT Frontier*, Springer Nature, Cham, Switzerland, **2017**.
[3] P. K. Murali, M. Kaboli, R. Dahiya, *Adv. Intell. Syst.* **2022**, *4*, 2100122.
[4] G. P. Fettweis, *IEEE Veh. Technol. Mag.* **2014**, *9*, 64.
[5] C. (IDC) MacGillivray, V. (IDC) Turner, *Worldwide Internet of Things Forecast, 2015–2020*, International Data Corporation (IDC), Framingham, MA **2015**, p. 15.
[6] S. K. Ghosh, D. Mandal, *Nano Energy* **2018**, *53*, 245.
[7] J. Jiang, S. Tu, R. Fu, J. Li, F. Hu, B. Yan, Y. Gu, S. Chen, *ACS Appl. Mater. Interfaces* **2020**, *12*, 33989.
[8] A. Spanu, L. Pinna, F. Viola, L. Seminara, M. Valle, A. Bonfiglio, P. Cosseddu, *Org. Electron.* **2016**, *36*, 57.
[9] Y. Liu, R. Bao, J. Tao, J. Li, M. Dong, C. Pan, *Sci. Bull.* **2020**, *65*, 70.
[10] E. Kar, N. Bose, B. Dutta, N. Mukherjee, S. Mukherjee, *ACS Appl. Mater. Interfaces* **2019**, *11*, 17501.
[11] D. B. Deutz, N. T. Mascarenhas, J. B. J. Schelen, D. M. de Leeuw, S. van der Zwaag, P. Groen, *Adv. Funct. Mater.* **2017**, *27*, 1700728.
[12] R. Ahmed, F. Mir, S. Banerjee, Y. Qin, T. Wei, Y. Zhao, M. Safaei, H. A. Sodano, S. R. Anton, *Smart Mater. Struct.* **2019**, *28*, 113001.
[13] N. A. Shepelin, A. M. Glushenkov, V. C. Lussini, P. J. Fox, G. W. Dicinoski, J. G. Shapter, A. V. Ellis, *Energy Environ. Sci.* **2019**, *12*, 1143.
[14] Y. Sun, J. Chen, X. Li, Y. Lu, S. Zhang, Z. Cheng, *Nano Energy* **2019**, *61*, 337.

[15] M. M. Abolhasani, M. Naebe, M. Hassanpour Amiri, K. Shirvanimoghaddam, S. Anwar, J. J. Michels, K. Asadi, *Adv. Sci.* **2020**, *7*, 2000517.

[16] X. Liao, Q. Liao, Z. Zhang, X. Yan, Q. Liang, Q. Wang, M. Li, Y. Zhang, *Adv. Funct. Mater.* **2016**, *26*, 3074.

[17] D. S. Kwon, H. J. Ko, M. O. Kim, Y. Oh, J. Sim, K. Lee, K. H. Cho, J. Kim, *Appl. Phys. Lett.* **2014**, *104*, 113904.

[18] H. B. Song, I. Karakurt, M. Wei, N. Liu, Y. Chu, J. Zhong, L. Lin, *Nano Energy* **2018**, *49*, 7.

[19] L. Jin, S. Ma, W. Deng, C. Yan, T. Yang, X. Chu, G. Tian, D. Xiong, J. Lu, W. Yang, *Nano Energy* **2018**, *50*, 632.

[20] Q. Sun, W. Seung, B. J. Kim, S. Seo, S. W. Kim, J. H. Cho, *Adv. Mater.* **2015**, *27*, 3411.

[21] R. Sun, S. C. Carreira, Y. Chen, C. Xiang, L. Xu, B. Zhang, M. Chen, I. Farrow, F. Scarpa, J. Rossiter, *Adv. Mater. Technol.* **2019**, *4*, 1900100.

[22] W. Wang, P. N. Stipp, K. Ouaras, S. Fathi, Y. Yan Shery Huang, W. Wang, P. N. Stipp, K. Ouaras, S. Fathi, Y. Y. S Huang, *Small* **2020**, *16*, 2000581.

[23] Y. H. Jung, S. K. Hong, H. S. Wang, J. H. Han, T. X. Pham, H. Park, J. Kim, S. Kang, C. D. Yoo, K. J. Lee, *Adv. Mater.* **2020**, *32*, 1904020.

[24] Y. Q. Fu, J. K. Luo, N. T. Nguyen, A. J. Walton, A. J. Flewitt, X. T. Zu, Y. Li, G. McHale, A. Matthews, E. Iborra, H. Du, W. I. Milne, *Prog. Mater. Sci.* **2017**, *89*, 31.

[25] S. Park, X. Guan, Y. Kim, F. (Pete) X. Creighton, E. Wei, I. Kymissis, H. H. Nakajima, E. S. Olson, *Trends Hear* **2018**, *22*, 2331216518774450.

[26] T. H. Lee, C. Y. Chen, C. Y. Tsai, Y. K. Fuh, *Polymers* **2018**, *10*, 692.

[27] W. Deng, Y. Zhou, A. Libanori, G. Chen, W. Yang, J. Chen, *Chem. Soc. Rev.* **2022**, *51*, 3380.

[28] J. C. Meyer, A. K. Geim, M. I. Katsnelson, K. S. Novoselov, T. J. Booth, S. Roth, *Nature* **2007**, *446*, 60.

[29] X. Wang, A. M. Jones, K. L. Seyler, V. Tran, Y. Jia, H. Zhao, H. Wang, L. Yang, X. Xu, F. Xia, *Nat. Nanotechnol.* **2015**, *10*, 517.

[30] L. Li, Y. Yu, G. J. Ye, Q. Ge, X. Ou, H. Wu, D. Feng, X. H. Chen, Y. Zhang, *Nat. Nanotechnol.* **2014**, *9*, 372.

[31] L. Ding, Y. Wei, L. Li, T. Zhang, H. Wang, J. Xue, L. X. Ding, S. Wang, J. Caro, Y. Gogotsi, *Nat Commun* **2018**, *9*, 155.

[32] X. Wang, S. Kajiyama, H. Iinuma, E. Hosono, S. Oro, I. Moriguchi, M. Okubo, A. Yamada, *Nat. Commun.* **2015**, *6*, 1.

[33] R. Roldán, A. Castellanos-Gomez, E. Cappelluti, F. Guinea, *J. Phys. Condens. Matter* **2015**, *27*, 313201.

[34] P. Di Pietro, M. Ortolani, O. Limaj, A. Di Gaspare, V. Giliberti, F. Giorgianni, M. Brahlek, N. Bansal, N. Koirala, S. Oh, P. Calvani, S. Lupi, *Nat. Nanotechnol.* **2013**, *8*, 556.

[35] M. X. Wang, C. Liu, J. P. Xu, F. Yang, L. Miao, M. Y. Yao, C. L. Gao, C. Shen, X. Ma, X. Chen, Z. A. Xu, Y. Liu, S. C. Zhang, D. Qian, J. F. Jia, Q. K. Xue, *Science* **2012**, *335*, 52.

[36] C. Cui, W.-J. Hu, X. Yan, C. Addiego, W. Gao, Y. Wang, Z. Wang, L. Li, Y. Cheng, P. Li, X. Zhang, H. N. Alshareef, T. Wu, W. Zhu, X. Pan, L.-J. Li, *Nano Lett.* **2018**, *18*, 1253.

[37] J. O. Island, S. I. Blanter, M. Buscema, H. S. J. Van Der Zant, A. Castellanos-Gomez, *Nano Lett.* **2015**, *15*, 7853.

[38] A. H. Woomer, T. W. Farnsworth, J. Hu, R. A. Wells, C. L. Donley, S. C. Warren, *ACS Nano* **2015**, *9*, 8869.

[39] N. Youngblood, C. Chen, S. J. Koester, M. Li, *Nat. Photonics* **2015**, *9*, 247.

[40] K. Kim, J. Y. Choi, T. Kim, S. H. Cho, H. J. Chung, *Nature* **2011**, *479*, 338.

[41] F. A. Rasmussen, K. S. Thygesen, *J. Phys. Chem. C* **2015**, *119*, 13169.

[42] J. Quereda, R. Biele, G. Rubio-Bollinger, N. Agraït, R. D'Agosta, A. Castellanos-Gomez, *Adv. Opt. Mater.* **2016**, *4*, 1939.

[43] M. Dai, Z. Wang, F. Wang, Y. Qiu, J. Zhang, C.-Y. Xu, T. Zhai, W. Cao, Y. Fu, D. Jia, Y. Zhou, P.-A. Hu, *Nano Lett.* **2019**, *19*, 5410.

[44] K. Rogdakis, N. Karakostas, E. Kymakis, *Energy Environ. Sci.* **2021**, *14*, 3352.

[45] M. Dai, H. Chen, F. Wang, Y. Hu, S. Wei, J. Zhang, Z. Wang, T. Zhai, P. A. Hu, *ACS Nano* **2019**, *13*, 7291.

[46] F. Xue, X. He, J. R. D. Retamal, A. Han, J. Zhang, Z. Liu, J. K. Huang, W. Hu, V. Tung, J. H. He, L. J. Li, X. Zhang, *Adv. Mater.* **2019**, *31*, 1901300.

[47] S. Witomska, T. Leydecker, A. Ciesielski, P. Samorì, *Adv. Funct. Mater.* **2019**, *29*, 1901126.

[48] M. S. Claro, J. Grzonka, N. Nicoara, P. J. Ferreira, S. Sadewasser, *Adv. Opt. Mater.* **2021**, *9*, 2001034.

[49] W. Li, M. Dai, Y. Hu, H. Chen, X. Zhu, Q. Yang, P. Hu, *ACS Appl. Mater. Interfaces* **2019**, *11*, 47098.

[50] P. K. Mohapatra, K. Ranganathan, L. Dezanashvili, L. Houben, A. Ismach, *Appl. Mater. Today* **2020**, *20*, 100734.

[51] W. Feng, W. Zheng, F. Gao, X. Chen, G. Liu, T. Hasan, W. Cao, P. Hu, *Chem. Mater.* **2016**, *28*, 4278.

[52] S. Aftab, H. H. Hegazy, *Small* **2023**, *19*, 2205778.

[53] Y. Zhao, F. Guo, R. Ding, W. F. Io, S. Y. Pang, W. Wu, J. Hao, *Adv. Opt. Mater.* **2021**, *9*, 2100864.

[54] W. Cai, J. Wang, Y. He, S. Liu, Q. Xiong, Z. Liu, Q. Zhang, *Nano-Micro Lett.* **2021**, *13*, 74.

[55] M. Wang, F. Cao, L. Meng, W. Tian, L. Li, *Adv. Mater. Interfaces* **2019**, *6*, 1801526.

[56] Z. Zheng, P. Chen, J. Lu, J. Yao, Y. Zhao, M. Zhang, M. Hao, J. Li, *Sci. China Mater.* **2020**, *63*, 1560.

[57] Y. Wang, S. Liu, Q. Li, G. Wu, X. Wang, P. Wang, W. Feng, F. Gao, Y. Hu, M. Dai, H. Li, L. Wang, P. Hu, *Nanotechnology* **2018**, *29*, 445205.

[58] L. Tang, C. Teng, Y. Luo, U. Khan, H. Pan, Z. Cai, Y. Zhao, B. Liu, H.-M. Cheng, **2019**.

[59] P. Hou, Y. Lv, Y. Chen, Y. Liu, C. Wang, P. Zhou, X. Zhong, J. Wang, X. Ouyang, *ACS Appl. Electron. Mater.* **2020**, *2*, 140.

[60] Y. Hu, W. Feng, M. Dai, H. Yang, X. Chen, G. Liu, S. Zhang, P. Hu, *Semicond. Sci. Technol.* **2018**, *33*, 125002.

[61] W. Huang, M. Song, Y. Zhang, Y. Zhao, H. Hou, L. H. Hoang, X. Chen, *J. Alloys Compd.* **2022**, *904*, 164010.

[62] C. Jia, S. Wu, J. Fan, C. Luo, M. Fan, M. Li, L. He, Y. Yang, H. Zhang, *ACS Nano* **2023**, *17*, 6534.

[63] T. Yang, X. Jiang, Y. Huang, Q. Tian, L. Zhang, Z. Dai, H. Zhu, *iScience* **2022**, *25*, 103728.

[64] J. Qi, Y. W. Lan, A. Z. Stieg, J. H. Chen, Y. L. Zhong, L. J. Li, C. D. Chen, Y. Zhang, K. L. Wang, *Nat. Commun.* **2015**, *6*, 7430.

[65] R. Hinchet, U. Khan, C. Falconi, S. W. Kim, *Mater. Today* **2018**, *21*, 611.

[66] M. Huang, T. A. Pascal, H. Kim, W. A. Goddard, J. R. Greer, *Nano Lett.* **2011**, *11*, 1241.

[67] J. Fraden, *Handbook of Modern Sensors: Physics, Designs and Applications*, Springer International Publishing, Cham, Switzerland **2016**, p. 1.

[68] J. Cao, Q. Wang, H. Dai, *Phys. Rev. Lett.* **2003**, *90*, 157601.

[69] O.-G. Hayber, *J. Nanoelectron. Optoelectron.* **2019**, *14*, 464.

[70] C. Zheng, L. Yu, L. Zhu, J. L. Collins, D. Kim, Y. Lou, C. Xu, M. Li, Z. Wei, Y. Zhang, M. T. Edmonds, S. Li, J. Seidel, Y. Zhu, J. Z. Liu, W. X. Tang, M. S. Fuhrer, *Sci. Adv.* **2018**, *4*, eaar7720.

[71] R. B. Jacobs-Gedrim, M. Shanmugam, N. Jain, C. A. Durcan, M. T. Murphy, T. M. Murray, R. J. Matyi, R. L. Moore, B. Yu, *ACS Nano* **2014**, *8*, 514.

[72] C. Zhu, H. Shen, H. Liu, X. Lv, Z. Li, Q. Yuan, *Chem. – Eur. J.* **2018**, *24*, 19060.

[73] S. Chen, X. Liu, X. Qiao, X. Wan, K. Shehzad, X. Zhang, Y. Xu, X. Fan, *Small* **2017**, *13*, 1604033.

[74] G. Almeida, S. Dogan, G. Bertoni, C. Giannini, R. Gaspari, S. Perissinotto, R. Krahne, S. Ghosh, L. Manna, *J. Am. Chem. Soc.* **2017**, *139*, 3005.

2300203 (11 of 12)

[75] S. Zhou, X. Tao, Y. Gu, *J. Phys. Chem. C* **2016**, *120*, 4753.

[76] H. Shi, M. Li, A. Shaygan Nia, M. Wang, S. Park, Z. Zhang, M. R. Lohe, S. Yang, X. Feng, H. Shi, M. Li, A. Shaygan Nia, M. Wang, S. Park, Z. Zhang, M. R. Lohe, S. Yang, X. Feng, *Adv. Mater.* **2020**, *32*, 1907244.

[77] Z. Y. Xia, G. Giambastiani, C. Christodoulou, M. V. Nardi, N. Koch, E. Treossi, V. Bellani, S. Pezzini, F. Corticelli, V. Morandi, A. Zanelli, V. Palermo, *ChemPlusChem* **2014**, *79*, 439.

[78] M. Si, A. K. Saha, S. Gao, G. Qiu, J. Qin, Y. Duan, J. Jian, C. Niu, H. Wang, W. Wu, S. K. Gupta, P. D. Ye, *Nat. Electron.* **2019**, *2*, 580.

[79] Y. Zhou, D. Wu, Y. Zhu, Y. Cho, Q. He, X. Yang, K. Herrera, Z. Chu, Y. Han, M. C. Downer, H. Peng, K. Lai, *Nano Lett.* **2017**, *17*, 5508.

[80] S. Logothetidis, A. Laskarakis, in *Solution-Processable Components of Organic Electronic Devices*, Vol. **12** (Eds: J. Ulanski, B. Luszczynska, K. Matyjaszewski) Wiley-VCH, Weinheim, Germany **2019**, p. 627.

[81] A. Politano, G. Chiarello, R. Samnakay, G. Liu, B. Gürbulak, S. Duman, A. A. Balandin, D. W. Boukhvalov, *Nanoscale* **2016**, *8*, 8474.

[82] L. Shi, Q. Zhou, Y. Zhao, Y. Ouyang, C. Ling, Q. Li, J. Wang, *J. Phys. Chem. Lett.* **2017**, *8*, 4368.

[83] K. J. Xiao, A. Carvalho, A. H. Castro Neto, *Phys. Rev. B* **2017**, *96*, 054112.

[84] E. J. Curry, K. Ke, M. T. Chorsi, K. S. Wrobel, A. N. Miller, A. Patel, I. Kim, J. Feng, L. Yue, Q. Wu, C. L. Kuo, K. W. H. Lo, C. T. Laurencin, H. Ilies, P. K. Purohit, T. D. Nguyen, *Proc. Natl. Acad. Sci. USA* **2018**, *115*, 909.

[85] J. Kim, M. Jang, G. Jeong, S. Yu, J. Park, Y. Lee, S. Cho, J. Yeom, Y. Lee, A. Choe, Y. R. Kim, Y. Yoon, S. S. Lee, K. S. An, H. Ko, *Nano Energy* **2021**, *89*, 106409.

[86] M. Hassanpour Amiri, R. Fatscher, R. Taylor, P. R. F. Rocha, C. R. Bowen, K. Asadi, *Nano Energy* **2023**, *106*, 108073.